

Unraveling the Voltage-Dependent Oxidation Mechanisms of Poly(Ethylene Oxide)-Based Solid Electrolytes for Solid-State Batteries

Lukas Seidl,* Rabeb Grissa, Leiting Zhang, Sigita Trabesinger, and Corsin Battaglia

Using galvanostatic techniques, an oxidative stability up to 4.6 V versus Li/Li⁺ and beyond has been reported for the prototypical polymer electrolyte consisting of 1 M lithium bis(trifluoromethanesulfonyl)imide (LiTFSI) in poly(ethylene oxide) (PEO). However, no long-term cycling of a battery with this high cut-off voltage has been demonstrated. Electrochemical and spectroscopic/spectrometric methods are employed to critically reinvestigate the electrochemical oxidation mechanisms of PEO electrolytes. It is found that the onset of PEO oxidation occurs at much lower voltage of around 3.2 V versus Li/Li⁺, at which the terminal O–H group is deprotonated. At 3.6 V, the chain of the PEO is oxidized. Both processes result in the formation of the strong acid HTFSI, which in turn chemically attacks the PEO to form methanol and 2-methoxyethanol. A stable cycling of a solid-state lithium-metal battery with a high-energy LiNi_{0.8}Mn_{0.1}Co_{0.1}O₂ (NMC811) positive electrode to an upper cut-off voltage of 3.6 V versus Li/Li⁺ is demonstrated, however, resulting in enhanced capacity fading when increasing the upper cut-off voltage to 3.8 V versus Li/Li⁺ or higher. Thus, operating PEO electrolytes beyond 3.6 V versus Li/Li⁺ requires protective layers at the positive electrode-electrolyte interface to prevent PEO oxidation.

1. Introduction

Solid-state lithium batteries promise higher energy density by replacing the graphite negative electrode by lithium metal and higher safety by replacing industry-standard liquid electrolytes based on carbonates having a near-room-temperature flashpoint by solid electrolytes.^[1,2] The requirements for solid electrolytes

are versatile: besides possessing high lithium-ion conductivity, the electrolyte has to be chemically and electrochemically stable to withstand reduction or oxidation potentials occurring in contact with Li metal or the positive electrode, respectively.^[3–5] Nevertheless, in most cases, electrolytes tend to react with the electrodes, ideally forming a passivating interphase layer, which is electronically insulating but ionically conducting.^[6–8] Among the different types of solid electrolytes, polymer electrolytes are particularly interesting due to their elastic properties, which can compensate volume changes of the active electrode materials during charging and discharging of the battery. In addition, many polymer electrolytes can be processed easily at low temperature (e.g., solution processing, extrusion, molding, etc.),^[9] and in a solvent free process.^[10]

The prototypical polymer electrolyte for lithium-ion batteries is lithium bis(trifluoromethanesulfonyl)imide (LiTFSI) in poly(ethylene oxide) (PEO).^[11] Despite many reports claiming an oxidative stability beyond 5.0 V versus Li/Li⁺ for PEO-based electrolytes,^[12,13] stable battery cycling has been restricted to positive electrode materials with low redox potentials, such as LiFePO₄ (LFP) with a redox potential of ca. 3.6 V versus Li/Li⁺. Motivated by enabling PEO-based solid-state lithium-ion batteries with higher energy LiNi_xMn_yCo_zO₂ (NMC, $x+y+z=1$) electrode materials, we reinvestigate PEO oxidation.

Typically, the electrochemical stability window (ESW) of electrolytes is measured by potential sweep methods, such as linear sweep/cyclic voltammetry (LSV/CV). One general issue coming along with voltage sweep techniques is the low signal to background ratio due to slow reaction kinetics and the absence of convection in the solid electrolyte. A solution to mitigate this problem is to maximize the electrode surface area.^[14–17] Aside of density functional theory (DFT) calculations,^[18–20] a few attempts have been made in literature to determine the electrochemical stability of electrolytes by other methods than LSV and CV. Those include electrochemical impedance spectroscopy (EIS)^[21,22] and reverse linear sweep voltammetry.^[23] By the use of galvanostatic techniques, the oxidative PEO stability was found to be 4.6 V versus a Li metal negative electrode.^[24,25] Nevertheless, long-term cycling of a Li | PEO | NMC battery has not yet been demonstrated.

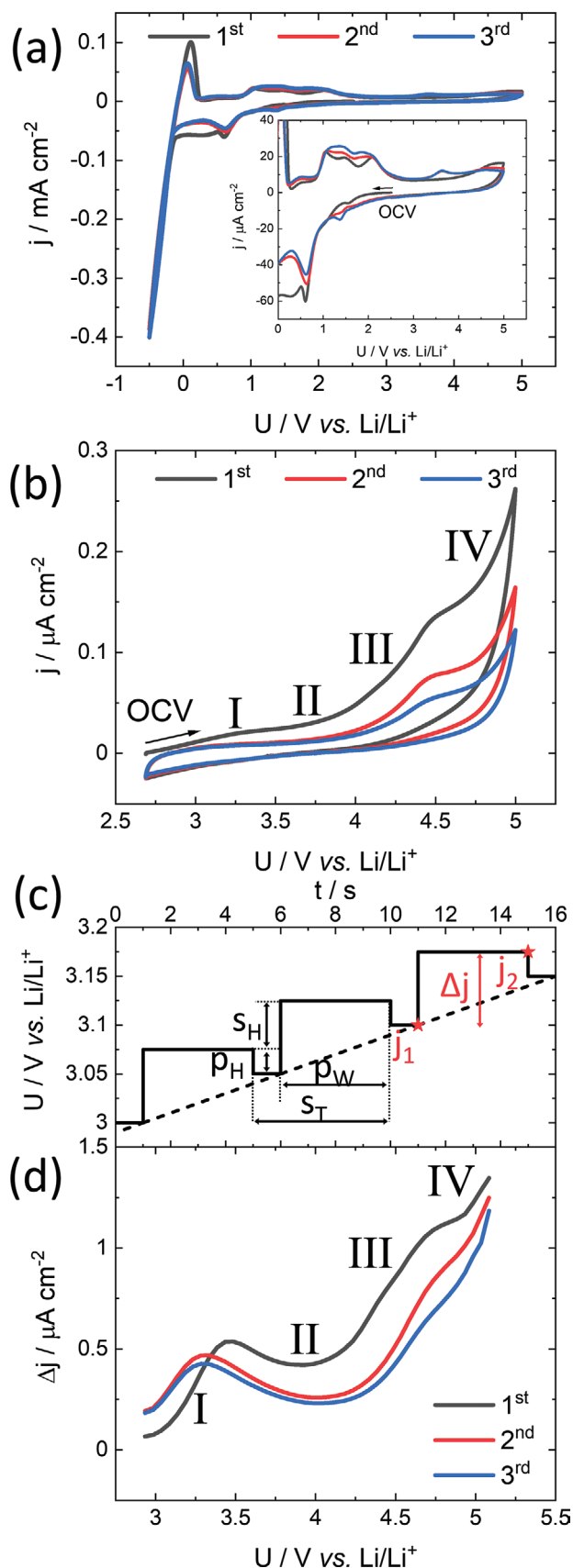
Dr. L. Seidl, Dr. R. Grissa, Dr. C. Battaglia
Empa – Swiss Federal Laboratories for Materials Science and Technology
Überlandstrasse 129, Dübendorf 8600, Switzerland
E-mail: lukas.seidl@empa.ch

Dr. L. Zhang, Dr. S. Trabesinger
Battery Electrodes and Cells
Electrochemistry Laboratory
Paul Scherrer Institute
Villigen PSI, Zürich 5232, Switzerland

 The ORCID identification number(s) for the author(s) of this article can be found under <https://doi.org/10.1002/admi.202100704>.

© 2021 The Authors. Advanced Materials Interfaces published by Wiley-VCH GmbH. This is an open access article under the terms of the Creative Commons Attribution License, which permits use, distribution and reproduction in any medium, provided the original work is properly cited.

DOI: 10.1002/admi.202100704



In this study, we combine several electrochemical and spectroscopic/spectrometric techniques, including cyclic voltammetry, differential pulse voltammetry (DPV), and EIS complemented by spectroscopic/spectrometric techniques including infrared spectroscopy, X-ray photoelectron spectroscopy, and mass spectrometry, to determine the oxidative stability limit of PEO-based electrolytes. We find that PEO oxidation occurs already at 3.2 V against a Li/Li⁺ counter electrode at the alcohol terminal groups. At 3.6 V the PEO chain is oxidized, resulting in the gradual loss of Li-ion conductivity. Cycling of a Li | PEO | NMC battery confirms these results.

2. Results and Discussion

2.1. Voltammetry

Figure 1a presents a typical CV measurement of a Li | 1 M LiTFSI in PEO_{200,000} | SS cell measured at 60 °C. A planar stainless steel electrode is chosen here to enable the study of the pure electrochemical oxidation avoiding any chemical oxidation source like O₂, either introduced as gas^[26] or by an oxide electrode material.^[22] A 1 M Li⁺ concentration is chosen to measure the voltages between the working electrode and the Li/Li⁺ counter electrode without Nernst shift correction. All voltages reported in the following denote the voltage difference between the working electrode and the Li-metal electrode. Note that voltages are reported herein rather than potentials, as we employed 2-electrode setups for experiments.^[27]

The CV measurement, shown in Figure 1a, starts at the open circuit voltage (OCV) after 2 h equilibration at open circuit at 60 °C (see inset) and proceeds towards negative voltages at a voltage sweep rate of 10 mV s⁻¹. Li plating starts to dominate below 0 V. At -0.5 V, the voltage sweep direction is reversed and the voltage is swept up across the Li stripping peak to 5.0 V until the first cycle is completed. Following the first cycle, two more cycles are scanned. Even though such CV measurements are often employed to extract the ESW of the electrolyte, there are several flaws and drawbacks of the measurement, as it was performed as in Figure 1a: i) The CV is only suitable to extract the reductive stability of the electrolyte from the first scan towards negative voltages, as the PEO molecules irreversibly decompose at the interface to the stainless steel electrode already during the first sweep to lower voltages. These reduction products may have a different oxidation stability than the pristine PEO electrolyte. Thus, the reductive and the oxidative electrolyte stability must always be studied independently;^[17] ii) Li plating and stripping is a very fast reaction and delivers much higher current densities than the electrolyte decomposition, which in case of solid electrolytes are very low due to slow reaction kinetics and the absence of convection in the solid electrolyte. Thus, the currents

Figure 1. Comparison of CV curves of a Li | 1 M LiTFSI in PEO_{200,000} | SS cell at 60 °C measured a) from OCV towards Li-plating/-stripping and up to 5.0 V at a voltage sweep rate of 10 mV s⁻¹ and b) from OCV up to 5.0 V at a voltage sweep rate of 0.1 mV s⁻¹. c) Voltage-time profile applied during DPV measurement. d) DPVs of a Li | 1 M LiTFSI in PEO_{200,000} | SS cell at 60 °C measured from OCV up to 5.0 V (pulse amplitude p_H = 25 mV, pulse width p_W = 1 s, step height s_H = 50 mV, step time s_T = 5 s)

related to electrolyte decomposition are typically several orders of magnitude smaller than those of the Li plating and stripping reaction. This results in an overestimation of their electrochemical stability; and iii) the CV measurement in Figure 1a was performed at a fast voltage sweep rate ν of 10 mV s^{-1} . While non-Faradaic currents, such as the double layer charging, scale linearly with ν , Faradaic currents scale with $\nu^{1/2}$ in the best case, (i.e., with electrolyte diffusion).^[28] Consequently, the signal to background ratio scales with $\nu^{-1/2}$ and thus gets worse at higher scan rates. This effect can be seen when comparing the CV scan measured at 10 mV s^{-1} in Figure 1a with the scan measured at 0.1 mV s^{-1} in Figure 1b. Here, the onset of irreversible anodic current is detected at a voltage slightly above 3.0 V, whereas this oxidative current is not visible at 10 mV s^{-1} in Figure 1a.

The CV in Figure 1b is a better example of how to evaluate the oxidative stability of electrolytes, as it avoids the negative sweep to the Li stripping and plating regime and is measured at a sufficiently low voltage sweep rate. The first oxidation reaction starts at a voltage slightly above 3.0 V (I). Three more oxidation reactions are detected (II to IV). All four reactions are irreversible, as they only appear in the first cycle and no corresponding reductive peaks are detected in the reverse sweep. However, CV cannot provide any additional information about these electrochemical reactions, and it needs to be obtained through complementary methods.

The signal to background ratio in voltammetry measurements can be improved employing DPV. Figure 1d shows a DPV measurement of a Li | 1 M LiTFSI in PEO_{200,000} | SS cell at 60 °C. The measurement starts at OCV and the voltage is swept up to 5.0 V. A first oxidation reaction is detected slightly above 3.0 V (I), followed by three further oxidation reactions starting below 3.8 V (II to IV), consistent with the CV measurement in Figure 1b. Finding

the onset voltage from the electrochemical data for reaction II is difficult, as the peaks of reaction I and II in Figure 1 overlap.

It is interesting to note that in the first sweep, the onset of the oxidation reaction I occurs at a more positive voltage than in consecutive sweeps. Moreover, the differential current decreases from sweep to sweep, indicating electrode passivation due to formation of a solid electrolyte interphase. This particular measurement only took 3 min per sweep and the exposure time of the electrolyte to high voltage remains relatively short. This is why the oxidation peaks are visible in all three sweeps, as one voltage sweep is not sufficient to complete electrolyte oxidation. Thus, DPV detects the same oxidation processes as a slow scan rate CV, but within 3 min (Figure 1d) instead of 12 h (Figure 1b) per cycle. The weak point of DPV compared to CV due to the fast measurement, however, is the loss of information whether reactions are reversible or not.

2.2. Electrochemical Impedance Spectroscopy

Another electrochemical technique to study the ESW of electrolytes is EIS. Since EIS is also sensitive to the interphase layer formed by chemical PEO reduction on the Li electrode, the Li | 1 M LiTFSI in PEO_{200,000} | SS coin cell was equilibrated for four days at 60 °C at open circuit prior to the voltage-dependent EIS measurement. After equilibration, a 2 h voltage hold at a specific voltage, starting from 2.1 V, was applied to the cell, followed by an EIS measurement from 10 kHz to 100 mHz. This procedure was repeated for stepwise increasing cell voltage (0.1 V steps).

Selected Nyquist plots of the EIS data are shown in Figure 2a,b. One recognizes an Ohmic resistance of $660 \Omega \text{ cm}^{-2}$

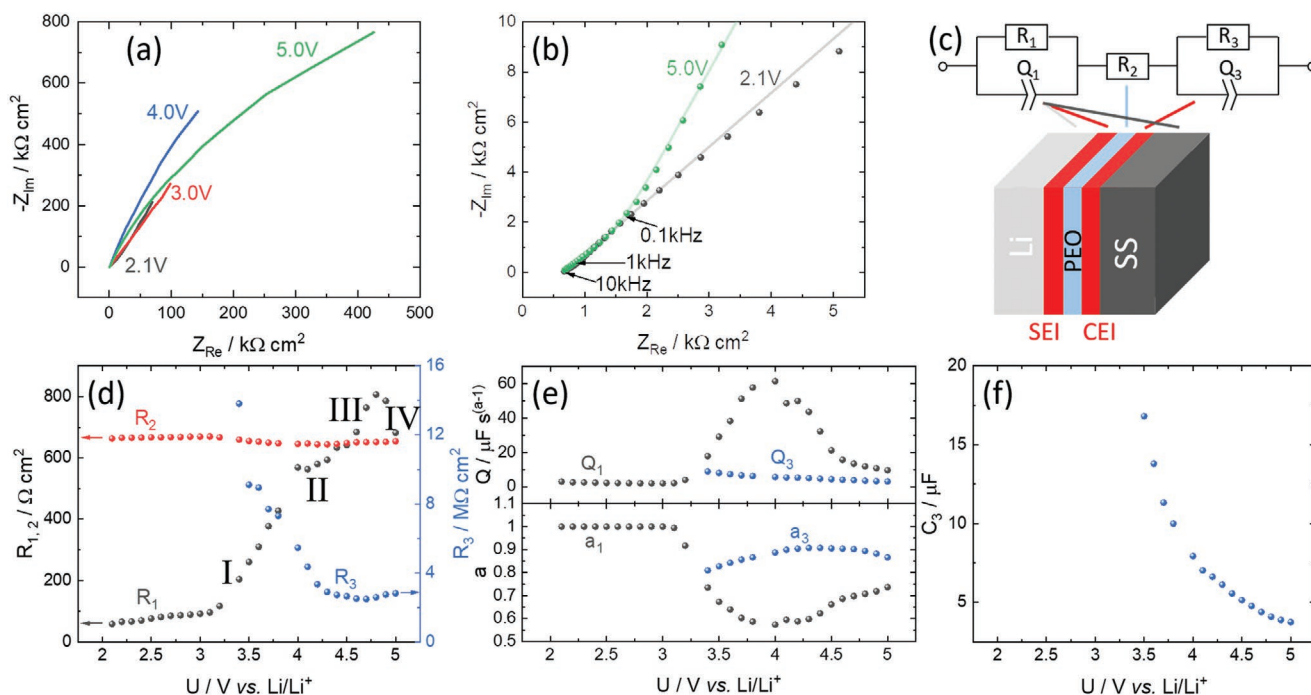


Figure 2. a) Nyquist plot of the electrochemical impedance data measured at 60 °C in a Li | 1 M LiTFSI in PEO_{200,000} | SS cell. The cell schematic with the corresponding equivalent circuit is shown in (c) and the obtained fit with the characteristic frequencies of the impedance spectra at 2.1 and 5.0 V, respectively, are shown in (b). The extracted fitting parameters are plotted as a function of voltage in (d–f). R denotes an Ohmic resistance, Q a constant phase element with the corresponding exponent a . The capacitance C_3 in (f) was calculated according to $C = (R \cdot Q)^{1/a}/R$.

at high frequencies and a contribution of a parallel R/Q -element at low frequencies, where R is a resistor and Q a constant phase element, which shows a voltage-dependent behavior. EIS data were fitted with an equivalent circuit shown in Figure 2c. The equivalent circuit consists of a parallel R/Q -element R_1/Q_1 connected in series with R_2 and a second parallel R/Q -element R_3/Q_3 . R_1/Q_1 represents the superposition of the resistances R_1 of the SS electrode and the Li electrode including the solid electrolyte interphase in parallel to a constant phase element Q_1 representing the electrochemical double layer at each electrode. R_2 is the electrolyte resistance and R_3/Q_3 represents the interphase layer formed due to PEO decomposition at the SS electrode. The R_3/Q_3 element results in an additional semicircle apparent in Figure 2a,b, which shows the impedance spectra of the fresh cell and after exposure to 5.0 V. The additional semicircle has a very high resistance ($M\Omega\text{ cm}^{-2}$) and appears at low frequency. According to literature,^[29] this additional semicircle cannot be attributed to the total electrical resistance of the formed interphase, as this would result in a significantly increased overvoltage and prevent charging and discharging of a battery. We attribute this behavior to an electronically conducting, but ionically almost blocking solid interphase formed at the blocking SS electrode.

Figure 2d,e shows all these parameters extracted from an equivalent circuit fitting as a function of electrode voltage. As expected, the electrolyte resistance R_2 remains constant as a function of voltage, as electrolyte oxidation affects only a very small region near the electrodes. Also the resistance R_1 remains constant at voltages below 3.2 V, below which the EIS data can be fitted without the need of R_3/Q_3 , as no passivating layer is yet present at the SS electrolyte interface. PEO oxidation is triggered around 3.2 V causing R_1 to increase and requiring a second R_3/Q_3 element for fitting to take into account oxidation-reaction products formed at the interface to the SS electrode. R_3 has values on the order of $M\Omega\text{ cm}^2$ and reaches a constant value of $1.3\text{ M}\Omega\text{ cm}^2$ at about 4.2 V. Q_1 on the other hand behaves like an ideal capacitor ($a_1 = 1$) for voltages below 3.2 V, but decreases significantly when PEO oxidation sets in above 3.2 V. The corresponding capacitance C_3 derived from R_3 , Q_3 and a_3 is plotted as a function of voltage in Figure 2f and amounts to several $\mu\text{F cm}^{-2}$. This is a typical value found for solid electrolyte interphases and confirms that the impedance

represented by the R_3/Q_3 element is caused by an interphase layer due to PEO oxidation at the positive electrode.^[30] Thus, while EIS delivers the same onset value for PEO oxidation at around 3.2 V as voltammetric techniques, it has the advantage of providing additional information on the transport properties of the decomposition products.

2.3. Fourier-Transform Infrared Spectroscopy

To identify the decomposition products formed during PEO oxidation on the SS electrode, we employ Fourier-transform infrared spectroscopy (FTIR). IR spectra measured post mortem on 1 M LiTFSI in PEO_{200,000} glass fiber separators extracted from Li | 1 M LiTFSI in PEO_{200,000} | SS cells as a function of applied voltage from 3.2 to 4.6 V are shown in Figure 3a (bright blue to grey spectra). The dark blue spectrum shows the IR spectrum of the electrolyte held at OCV.

The spectrum measured at 3.2 V is very similar to the spectrum measured at OCV. Increasing the voltage to 3.4 V, a reduction in the peak intensity at 1095 cm^{-1} corresponding to a $\text{C}-\text{O}_{\text{stretching}}$ mode (marked by the dashed circle) becomes apparent in the magnified view of the spectrum shown in Figure 3b. The onset voltage (between 3.2 and 3.4 V) is consistent with the onset for electrolyte oxidation (reaction I) determined by electrochemical techniques. The $\text{C}-\text{O}_{\text{stretching}}$ mode corresponds to the stretching vibration of the $\text{C}-\text{O}$ bond at the terminal $\text{C}-\text{OH}$ alcohol group.^[31,32] Thus, electrochemical oxidation starts at the alcohol terminal group of the PEO molecule.

The next voltage-induced changes in the IR spectra are observed after exposure to 3.6 V, affecting almost the entire spectrum. In the following, we highlight three major changes: i) The intensity of the peaks associated with the alcohol terminal group ($\text{C}-\text{O}_{\text{stretching}}$ at 1095 cm^{-1} and $\text{C}-\text{C}_{\text{alcohol}}$ at 875 cm^{-1}) strongly reduces to a point where the peak almost disappears; ii) the peak at 1050 cm^{-1} corresponding to an asymmetric $\text{S}-\text{N}-\text{S}$ vibration of the TFSI anion is replaced by a peak at 980 cm^{-1} , which can be assigned to the $\text{S}-\text{HN}-\text{S}$ vibration of an HTFSI molecule,^[33] formed by reaction of the TFSI⁻ anion with protons released during PEO oxidation.^[34] Moreover, new peaks appearing in the region around 1380 cm^{-1} stem from $\text{C}-\text{F}$, $\text{S}-\text{O}$, and $\text{C}-\text{S}$ vibrations in HTFSI, further confirming

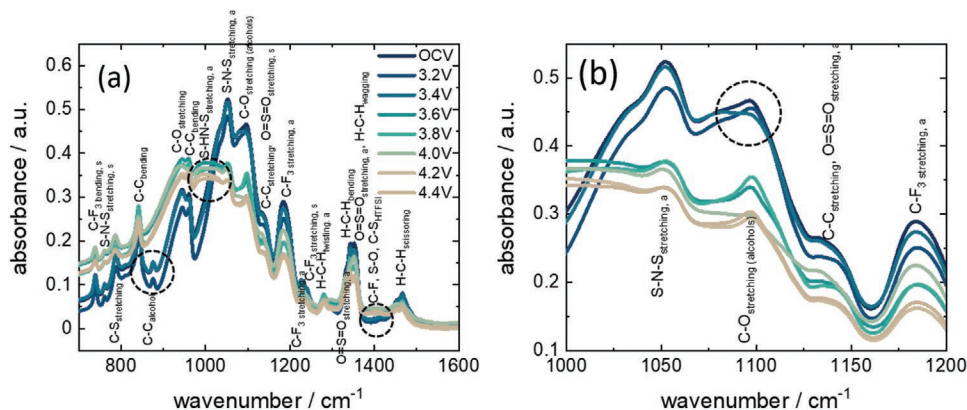


Figure 3. a) Post-mortem FTIR spectra of the 1 M LiTFSI in PEO_{200,000} glass fiber separator as a function of applied voltage with a literature-based assignment of the IR peaks.^[31,32,36,37] b) Magnified view onto the $\text{C}-\text{O}_{\text{stretching}}$ mode.

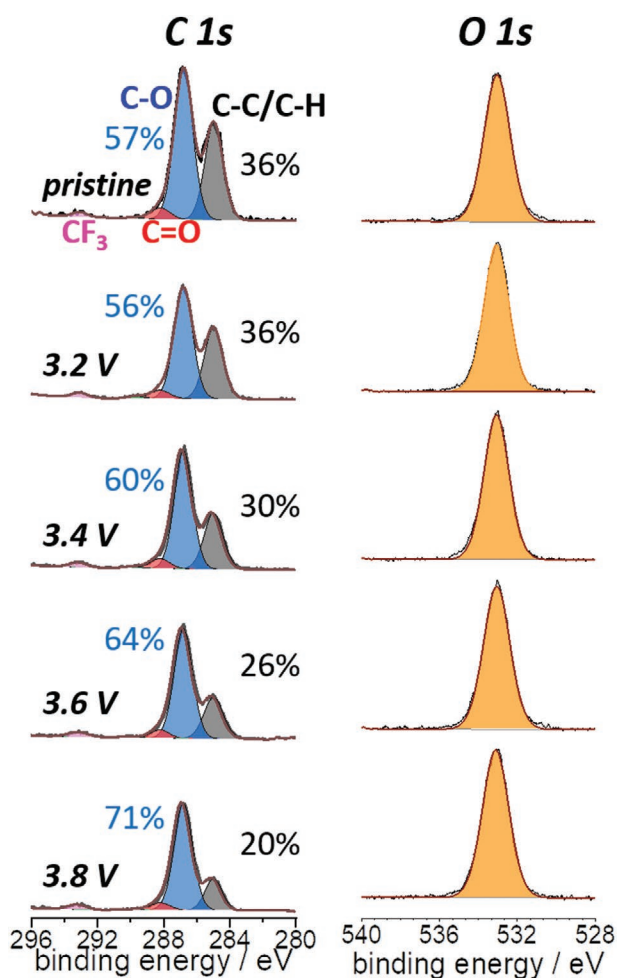


Figure 4. Post-mortem XPS spectra of the C 1s and the O 1s peaks of the 1 M LiTFSI in PEO_{200,000} glass fiber separator as a function of applied voltage. The first row corresponds to XPS data of a pristine sample not assembled into a cell. The black fitted C 1s peak originates from C–C carbon and C–H hydrocarbon contamination, the blue C 1s peak to C–O carbon, the red peak to C=O carbon, and the pink peak to CF₃ carbon from the LiTFSI salt.

the formation of HTFSI; iii) finally, also a gradual reduction of the peak intensity of C–C, C–O, and H–C–H vibrations is observed stemming from PEO chain oxidation into smaller fragments, occurring in parallel to HTFSI formation. Thus, reaction II at 3.6 V represents the oxidative decomposition of the PEO chain,^[35] accompanied by HTFSI formation.

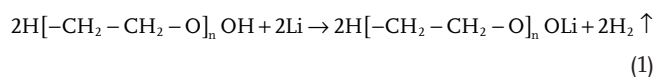
2.4. X-Ray Photoelectron Spectroscopy

Additional information on the PEO oxidation can be obtained from X-ray photoelectron spectroscopy (XPS). **Figure 4** shows post-mortem XPS spectra of the C 1s and the O 1s photoelectrons of the 1 M LiTFSI in PEO_{200,000} glass fiber separator as a function of applied voltage. The XPS spectra are normalized to the CF₃ related peak at 293.1 eV, as this peak is expected to remain unaffected during electrolyte oxidation. While the O 1s peaks remain unchanged for all samples, the C 1s peaks show

voltage dependent changes, mainly in the peak component at 285.0 eV (dark grey) associated with C–C and C–H bonds of PEO, but also with adventitious carbon contamination.^[38] The relative peak area of the C–C/C–H peak for the pristine sample amounts to 36% of the total C 1s peak area. The same value is found for the electrolyte exposed to 3.2 V. When the voltage is increased to 3.4, 3.6, and 3.8 V, the area of C–C/C–H component linearly decreases to 30%, 26%, and 20%, being an evidence for oxidation of the ether chain of PEO (reaction II). As the relative C–C/C–H peak intensities decrease the C–O peak increases to sum up to a total of 100%. The sensitivity of XPS is not sufficient to detect the oxidation of the alcohol terminal group in PEO with such long ether chains (reaction I), as the peak area associated with C–O bonds at 286.9 eV (blue) remains unchanged at 3.2 V. On the other hand, XPS detects the onset of PEO chain oxidation (reaction II) at 3.4 V, hinting to a higher sensitivity of XPS compared to FTIR to detect the onset.

2.5. Online Electrochemical Mass Spectrometry

Gases evolving from the cell due to the PEO oxidation can be measured using online electrochemical mass spectrometry (OEMS). A comparison of overview mass spectra measured on the Li | 1 M LiTFSI in PEO_{200,000} | SS cells held at open circuit and exposed to 5 V is shown in **Figure 5a**. The mass spectrum at open circuit (black spectrum) was measured after equilibrating the cell for 5 days at 60 °C and collecting the gases resulting from the chemical reaction of PEO with the Li electrode. This reaction results in the detection of atomic and molecular hydrogen at *m/z* 2 according to the decomposition reaction:



In a second step, the cell voltage was increased at a rate of 100 μV s^{−1} and the gas produced in the cell was sampled every 2 h by the mass spectrometer until reaching 5 V (red spectrum). The hydrogen peak at *m/z* 2 is still present. Moreover, the peaks in the *m/z* ranges 12–17, 22–34, and 42–46 increase significantly (note the logarithmic scale). Fragments are also found in the *m/z* range 60 and 77 (data not shown). The peaks at *m/z* 20, 36, 38, and 40 all belong to the Ar carrier gas and do not change when voltage is applied.

To understand the origin of these gases, reference spectra of different fragments of the PEO molecule are compared to the measured mass spectra. A good match is found for methanol and 2-methoxyethanol, shown in Figures 5b and 5c, respectively. Methanol produces the fragments found at *m/z* equal 2 as well as in the *m/z* range from 12–19 and 28–34. 2-methoxyethanol generates fragments in the *m/z* range 13–17, at 19, and 25–33, 41–48, and 60–77 (data only shown up to *m/z* = 50).

In order to determine the oxidative stability of PEO, OEMS measurements were performed by tracking selected *m/z* channels during the voltage ramp from OCV to 5 V. The applied voltage ramp (15 μV s^{−1}, black curve) and the resulting current density (blue curve) are shown in Figure 5d as a function of

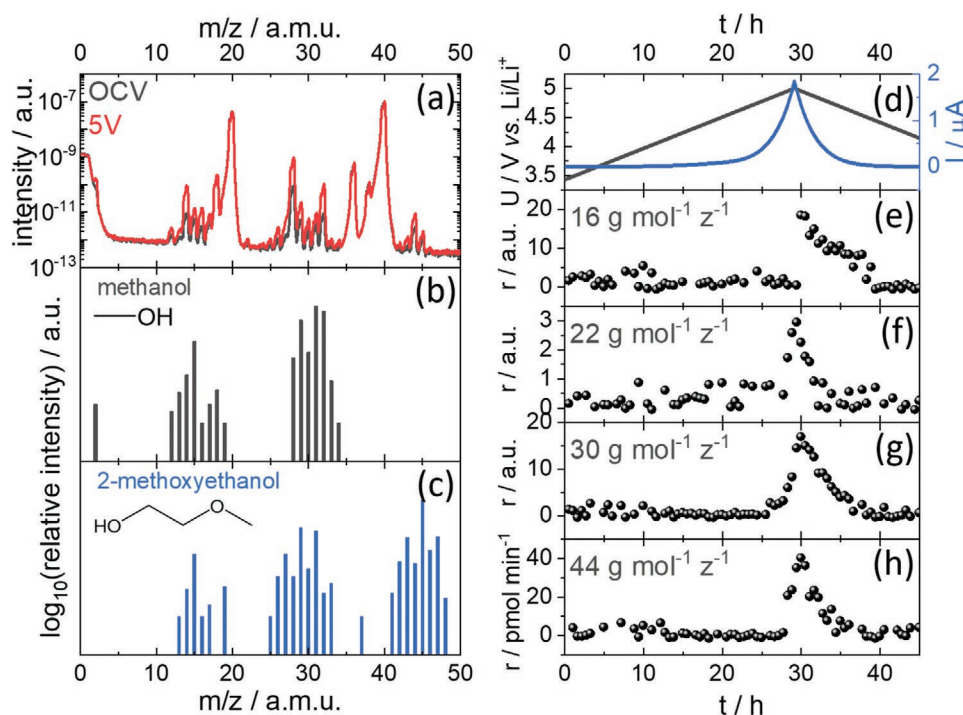


Figure 5. OEMS analysis of the 1 M LiTFSI in PEO_{200,000} glass fiber separator at 60 °C. a) Overview mass spectrum of the Li | 1 M LiTFSI in PEO_{200,000} | SS cell kept at OCV for 5 days (black curve) and after applying a voltage of 5 V between Li/Li⁺ (red curve). b,c) are reference spectra from literature^[39] of methanol ($m/z = 32$) and 2-methoxyethanol ($m/z = 76$, data only shown up to $m/z = 50$ for clarity), respectively, and/or their corresponding fragments. An automatic sequenced OEMS experiment is shown in d–h) with the applied voltage U (grey) and the resulting current I (blue) in (d), and the gas production rates r of the selected m/z channels at 16, 22, 30, and 44, respectively.

time. Figure 5e–h shows the production rates of gas fragments at m/z of 16, 22, 30, and 44 sampled every 45 min until reaching 5 V. A clear response to high voltages of each of these fragments is visible, however, the voltage sensitivity of OEMS compared to the methods presented above is reduced. Fragments at m/z of 16 for instance are only detected at 5 V, while fragments at m/z of 22 and 44 are detected at 4.9 V. The earliest response is seen at m/z of 30 at 4.8 V. Such a limitation is most likely owing to trace amount of decomposition products formed inside the cell during each sampling interval. A higher gas sensitivity could also be achieved for OEMS by collecting the gases over a longer period of time, while holding an applied voltage

instead of applying a voltage ramp, so does not represent an intrinsic limitation.

2.6. Electrochemical PEO Oxidation Mechanism

We now summarize the mechanism of PEO oxidation. FTIR spectroscopy indicates that the alcohol terminal group of the PEO molecule, oxidized at 3.2 V, is responsible for the onset of oxidation current in the electrochemical measurements (reaction I). The proposed reaction scheme is shown in **Figure 6**. First, the PEO molecule loses an electron at the O–H

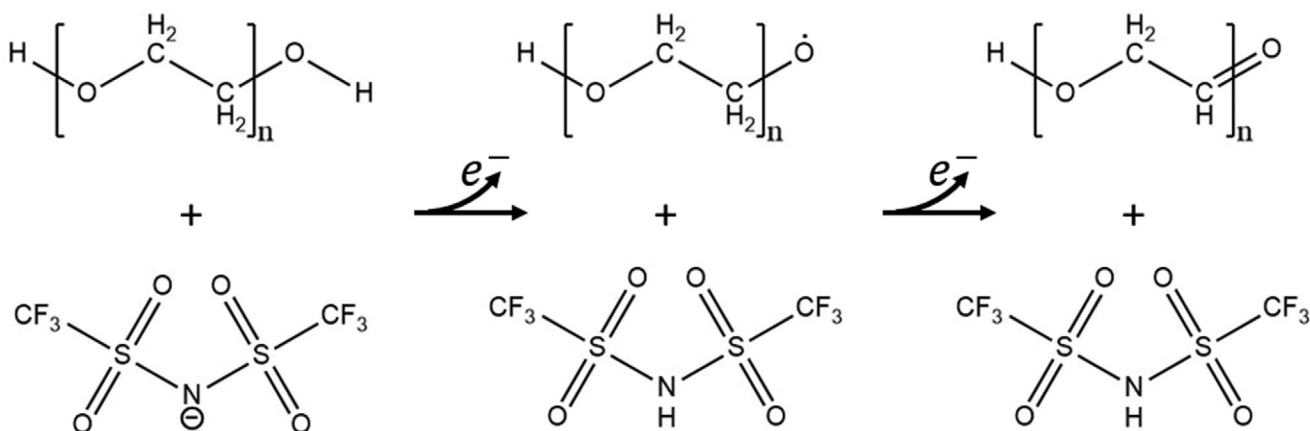


Figure 6. Oxidation mechanism of the PEO terminal group.

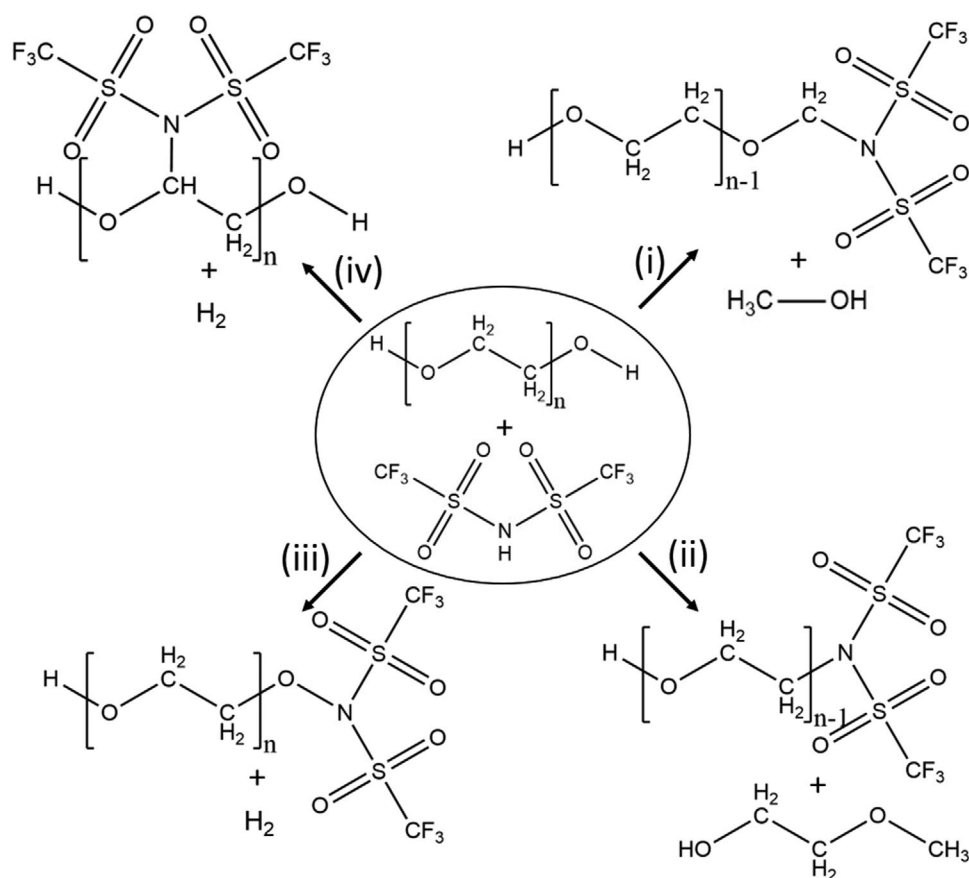


Figure 7. Refined reaction mechanism of the chemical reaction of HTFSI and PEO based on a theoretical study by Faglioni et al.^[41]

bond, which forms a PEO-radical and releases a proton. The proton is then captured by the TFSI anion to form the strong bis(trifluoromethanesulfonyl)imide acid (HTFSI). One should keep in mind that, even though it is a strong acid, HTFSI formation, unlike in a chemical reaction, can be forced in an electrochemical reaction. In a second electron transfer, the PEO loses another electron and another proton from a H–C–H group and forms a double bond to the oxygen at the terminal group. Yang et al.^[40] recently replaced the alcohol C–OH terminal group of PEO by a methyl C–OCH₃ group employing poly(ethylene glycol)dimethyl ether (PEGDME), enabling relatively stable cycling of a NMC cathode due to the enhanced oxidative stability.

Our measurements indicate that the more stable ether chain of the PEO molecule starts to be oxidized at more positive voltages (reaction II) than the terminal group (reaction I) in the range from 3.4 to 3.6 V resulting in enhanced HTFSI production. Similar observations employing composite electrodes at voltages >4.2 V were already made earlier, where an HTFSI crossover to the Li-electrode is proposed to result in H₂ formation.^[34] Faglioni et al.^[41] studied the mechanism of PEO chain oxidation in detail with density functional theory (DFT) and also considered the chemical reaction of HTFSI with the PEO molecules. Several potential reaction pathways were identified among which, one proposed pathway shown in **Figure 7**, predicts the formation of methanol (i), 2-methoxyethanol (ii), and H₂ (iii and iv). According to this theoretical study, the formation

of methanol and 2-methoxyethanol is equally favorable, while H₂ evolution is less probable. The predictions are in excellent agreement with our OEMS results, as H₂ is also generated during methanol fragmentation in the mass spectrometer (see reference spectrum in Figure 5b).

2.7. Cell Cycling Stability

The ultimate stability test for an electrolyte should always be the demonstration of stable cycling in contact with relevant electrode materials. **Figure 8a** shows the charge-discharge profiles of a Li | 1 M LiTFSI in PEO_{200,000} | NMC811 full cell polymer battery operated at 60 °C. NMC811 possesses a sloping voltage profile and can be delithiated to different upper cut-off voltages ranging from 3.6 to 4.6 V. As expected, the specific capacity of the cell increases with increasing cut-off voltage reaching a maximum second-cycle discharge capacity of 117 mAh g⁻¹ at 4.4 V (purple curve). Note the cumulative capacity loss of about 50 mAh g⁻¹ during previous cycles. Increasing the upper cut-off voltage to 4.6 V leads to a much lower second-cycle discharge capacity due to rapid electrolyte oxidation.

More important than the first-cycle discharge capacity is the evolution of the discharge capacity during prolonged cycling shown in **Figure 8b** for consecutively higher upper cut-off voltages. At an upper cut-off voltage of 3.6 V, no fading is observed

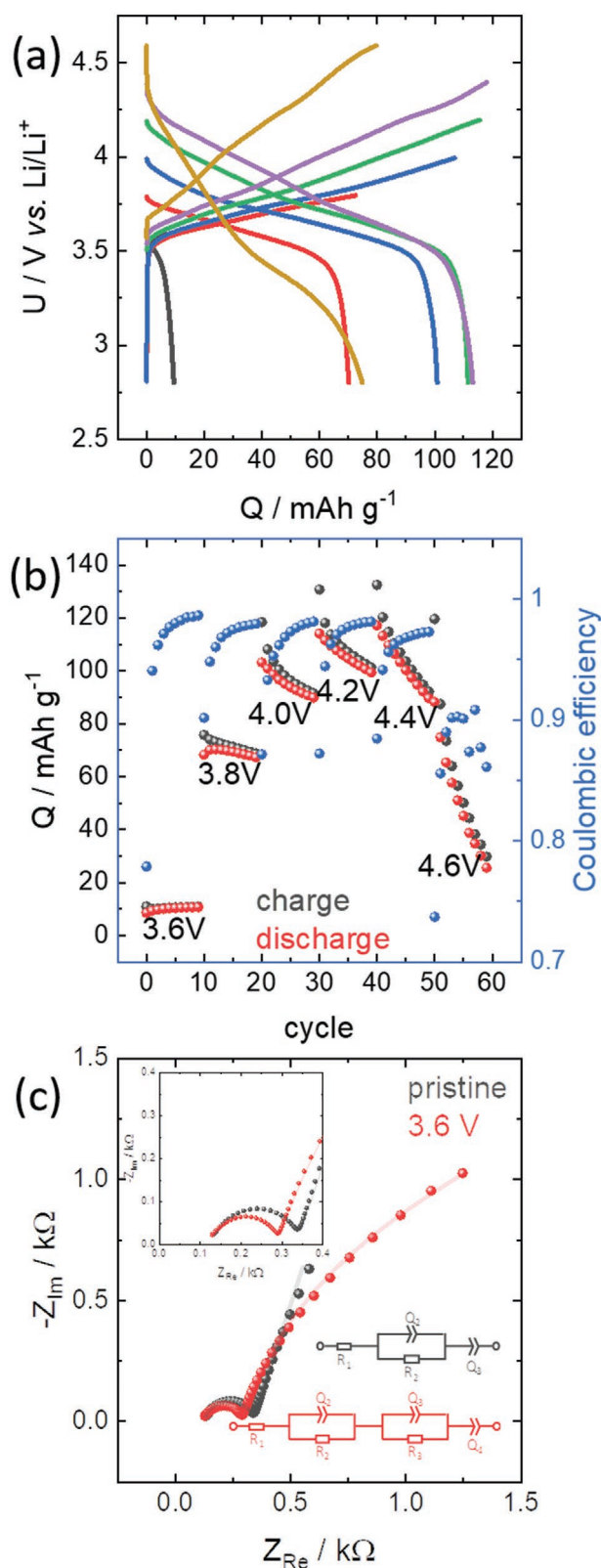


Figure 8. a) Charge/discharge profiles of a $\text{Li}|1\text{ m LiTFSI in PEO}_{200,000}|\text{NMC811}$ battery cycled at $C/10$ to different upper cut-off voltages. The charge/discharge capacities and the resulting Coulombic efficiencies as a function of cycle number are shown in (b). The EIS spectra with

during the first 10 cycles. In fact, the capacity even slightly increases as the contact between NMC811 particles and the PEO improves during the first cycles. Slight capacity fading sets in when cycling the cell to 3.8 V and increases rapidly as the upper cut-off voltage is increased further.

Cells shown here were cycled at a relatively low cycling rate of $C/10$, which promotes electrolyte oxidation beyond the onset voltage for PEO oxidation at 3.2 V. Cycling the cell at even lower cycling rate or subjecting the cell to a constant voltage above the oxidation onset would accelerate PEO oxidation further. However, electrolyte decomposition can be detected already before capacity fading becomes apparent employing EIS. Figure 8c shows Nyquist plots of a pristine cell and a cell cycled for 10 cycles at $C/10$ to an upper cut-off voltage of 3.6 V. Although no capacity fading is observed after this protocol, the Nyquist plots of the pristine cell (black curve) and the cycled cell (red curve) look clearly different. The impedance spectrum of the pristine cell can be fitted with an equivalent circuit consisting of the cell resistance R_1 , as well as an interface resistance R_2 in parallel to a constant phase element Q_2 and another serial constant phase element Q_3 . The impedance spectrum of the cycled cell, however, can only be fitted with an additional R/Q element representing an additional interphase layer formed by PEO oxidation on the NMC811 electrode. This is consistent with the above observations, where the onset voltage of the PEO chain oxidation is found at around 3.6 V. Thus, operating a PEO-based battery beyond 3.6 V results in a reduced cycle life, as the electrolyte is steadily decomposed.

3. Conclusion

In conclusion, we demonstrated that the onset of PEO oxidation on stainless steel electrodes occurs at a voltage of 3.2 V against a Li counter electrode (reaction I). At this voltage, the alcohol terminal group of PEO is deprotonated and forms the strong acid HTFSI. HTFSI reacts chemically with the ether chain of PEO resulting in the formation of methanol and 2-methoxyethanol consistent with one of the pathways proposed by theoretical calculations.^[41] At higher voltages around 3.6 V, the ether chain of the PEO is oxidized (reaction II) and accelerates HTFSI formation. Thus, PEO-based electrolytes are compatible with electrode materials having a redox potential below 3.6 V versus Li/Li^+ , for instance LFP. At higher voltages, the PEO-chain, which is responsible for the Li-ion transport, is destroyed gradually, resulting in performance degradation of NMC-PEO batteries. In order to increase the energy density of PEO-based solid-state lithium batteries, one can either use low-voltage/high-capacity positive electrode materials or try to prevent PEO oxidation by protective coatings of high-voltage positive electrodes, as coatings serve to reduce the potential to which the electrolyte is exposed to and hamper electron transfer kinetics.^[42]

the corresponding equivalent circuits of the pristine cell (grey) and the cell after 10 cycles with a cut-off voltage of 3.6 V (red) are shown in (c). The continuous line shows the fits with the drawn equivalent circuits.

4. Experimental Section

The polymer electrolyte was prepared by mixing LiTFSI (99.95%, anhydrous, Sigma Aldrich) and poly(ethylene oxide) (M_w : 200,000 g mol⁻¹, Sigma Aldrich). The LiTFSI/PEO_{200,000} ratio was adjusted to obtain 1 M LiTFSI in PEO_{200,000}, using a PEO mass density of 1.21 g cm⁻³ for calculations. The powder mixture was fully dissolved in acetonitrile (ACN, 99.8%, anhydrous, Sigma Aldrich) and stirred with a magnetic stirrer for several hours. Afterwards, the LiTFSI-PEO solution was drop cast on a glass fiber separator (Whatman, GF/A) using a glass plate as support. After completely absorbing the solution, the Whatman filter was transferred to an oven for drying at 60 °C for 1 h. Once the ACN evaporated, disks with a diameter of 16 mm were punched from the PEO-impregnated glass fiber separator for coin cell assembly. The polymer electrolyte disks were subsequently dried in vacuum for 12 h at 50 °C, and handled in an Ar-filled glovebox afterwards. Note that the glass fiber separator has high oxidative stability (>4.5 V versus Li/Li⁺)^[43] and serves as an electrochemically inactive spacer between the two electrodes to prevent a short circuit when the polymer electrolyte softens and creeps under the applied cell pressure at elevated temperatures.^[44]

NMC electrodes were prepared in an analogous way as the separators, but by adding the electrode material LiNi_{0.8}Mn_{0.1}Co_{0.1}O₂ (NMC811, MSE) and conductive carbon (SuperC65, Timcal) to the 1 M LiTFSI/PEO_{200,000} mixture before the addition of ACN. The mixing ratios were 70%_{wt} of NMC811, 20%_{wt} of 1 M LiTFSI/PEO_{200,000} and 10%_{wt} of SuperC65. The addition of the electrolyte into the composite electrode was necessary, as the electrolyte was bound in the glass fiber separator and does not creep into the electrode to contact the active material. ACN was subsequently added to obtain a slurry, which was stirred by a magnetic stirrer for 1 h. Then, a 50 µm wet film of the slurry was coated on Al foil (15 µm thick) by an automatic coater (Sheen 1133N), before drying the coating at 60 °C in an oven in air. Next, 12 mm circular electrodes were punched, and compressed with roughly 500 MPa between two polished steel dies. To this step, the electrode preparation was done in air. Finally, the electrodes were vacuum dried in the same way as the electrolyte containing glass fiber separator above and handled in an Ar-filled glovebox afterwards. The resulting electrodes have a mass loading of about 1 mg cm⁻².

Electrochemical tests were performed in 2032 coin cells (MTI), which were assembled with a Li negative electrode (99.9%, 1 mm Alfa Aesar), the 1 M LiTFSI/PEO_{200,000} glass fiber separator versus either the stainless steel (SS) casing of the coin cell or the NMC811/PEO_{200,000} composite as positive electrode. The cells were operated at 60 °C with a Bio-Logic BCS 805 or a Bio-Logic VMP3 potentiostat. All cells were equilibrated at open circuit for 12 h at 60 °C before electrochemical measurements.

For post mortem FTIR (Bruker Alpha), multiple 2032 coin cells with a stainless steel casing as the working electrode, the 1 M LiTFSI/PEO_{200,000} glass fiber separator (16 mm diameter) and a Li negative counter electrode (16 mm diameter) were held at a specific voltage for 20 h at 60 °C after equilibration at open circuit for 22 h at 60 °C. Afterwards, the coin cells were disassembled in the glovebox and transferred to the spectrometer under Ar. IR spectra were recorded from the surface of the 1 M LiTFSI/PEO_{200,000} glass fiber separator that was in contact with the stainless steel electrode in attenuated total reflection (ATR) configuration in a frequency range from 400 to 4000 cm⁻¹ with a resolution of 4 cm⁻¹.

For post mortem XPS analysis, 1 M LiTFSI/PEO_{200,000} glass fiber separator samples were prepared analogously to the FTIR samples and transferred to the XPS system (PHI Quantum 2000, monochromated Al K_α radiation (1486.6 eV) with a pass energy of 30 eV), where each sample was analyzed on three different spots (150 µm diameter). The samples were exposed for a few seconds to air during the transfer from the Ar-filled sample container to the XPS loadlock. Sample charging was compensated employing a low energy electron gun. XPS spectra were calibrated by setting the hydrocarbon component of the C 1s photoemission peak to 285.0 eV binding energy and XPS data were processed with the CasaXPS software.

For OEMS, home-built OEMS cells were assembled in an Ar-filled glovebox using a stainless steel mesh as the positive electrode, a 1 M

LiTFSI/PEO_{200,000} glass fiber separator (22 mm diameter), and a Li metal counter electrode. Cells were subsequently equilibrated at open circuit at a temperature of 60 °C for 5 days, prior to cyclic voltammetry (CV) measurements from OCV to 5 V at a sweep rate of 15 µmV s⁻¹. Gaseous products were analyzed through a capillary connected to a quadrupole mass spectrometer (Pfeiffer Omnistar), calibrated using 1000 ppm CO₂ in Ar. The OEMS setup is described elsewhere.^[45]

Acknowledgements

This work was supported by the ICON project "IE4B", a joint initiative by Fraunhofer ISC and Empa.

Conflict of Interest

The authors declare no conflict of interest.

Data Availability Statement

Research data are not shared.

Keywords

electrochemical stability, Li-metal batteries, NMC electrodes, PEO oxidation mechanism, poly(ethylene oxide) (PEO), solid electrolytes, solid-state batteries

Received: April 29, 2021

Revised: May 21, 2021

Published online: July 30, 2021

- [1] J. Janek, W. G. Zeier, *Nat. Energy* **2016**, 1, 16141.
- [2] Z. Zhang, Y. Shao, B. Lotsch, Y. S. Hu, H. Li, J. Janek, L. F. Nazar, C. W. Nan, J. Maier, M. Armand, L. Chen, *Energy Environ. Sci.* **2018**, 11, 1945.
- [3] K. Xu, *Chem. Rev.* **2004**, 104, 4303.
- [4] J. Mindemark, M. J. Lacey, T. Bowden, D. Brandell, *Prog. Polym. Sci.* **2018**, 81, 114.
- [5] K. N. Jung, H. S. Shin, M. S. Park, J. W. Lee, *ChemElectroChem* **2019**, 6, 3842.
- [6] E. Peled, S. Menkin, *J. Electrochem. Soc.* **2017**, 164, A1703.
- [7] J. Kasnatscheew, M. Evertz, B. Streipert, R. Wagner, S. Nowak, I. C. Laskovic, M. Winter, *J. Phys. Chem. C* **2017**, 121, 1521.
- [8] R. Jung, M. Metzger, F. Maglia, C. Stinner, H. A. Gasteiger, *J. Phys. Chem. Lett.* **2017**, 8, 4820.
- [9] A. Manthiram, X. Yu, S. Wang, *Nat. Rev. Mater.* **2017**, 2, 16103.
- [10] G. Foran, D. Mankovsky, N. Verdier, D. Lepage, A. Pr  b  , D. Aym  -Perrot, M. Doll  , *iScience* **2020**, 23, 101597.
- [11] M. Armand, *Solid State Ionics* **1983**, 9–10, 745.
- [12] Y. Lin, Y. Cheng, J. Li, J. D. Miller, J. Liu, X. Wang, *RSC Adv.* **2017**, 7, 24856.
- [13] K. Q. He, J. W. Zha, P. Du, S. H. S. Cheng, C. Liu, Z. M. Dang, R. K. Y. Li, *Dalton Trans.* **2019**, 48, 3263.
- [14] K. Xu, S. P. Ding, T. R. Jow, *J. Electrochem. Soc.* **1999**, 146, 4172.
- [15] R. Asakura, L. Duch  ne, R. S. K  hnel, A. Remhof, H. Hagemann, C. Battaglia, *ACS Appl. Energy Mater.* **2019**, 2, 6924.
- [16] Y. Xia, T. Fujieda, K. Tatsumi, P. P. Prosini, T. Sakai, *J. Power Sources* **2001**, 92, 234.

- [17] F. Han, Y. Zhu, X. He, Y. Mo, C. Wang, *Adv. Energy Mater.* **2016**, 6, 1501590.
- [18] S. Pandian, S. P. Adiga, P. Tagade, K. S. Hariharan, K. S. Mayya, Y. G. Lee, *J. Power Sources* **2018**, 393, 204.
- [19] L. Chen, S. Venkatram, C. Kim, R. Batra, A. Chandrasekaran, R. Ramprasad, *Chem. Mater.* **2019**, 31, 4598.
- [20] C. F. N. Marchiori, R. P. Carvalho, M. Ebadi, D. Brandell, C. M. Araujo, *Chem. Mater.* **2020**, 32, 7237.
- [21] D. Chen, J. Cheng, Y. Wen, G. Cao, Y. Yang, H. Liu, *Int. J. Electrochem. Sci.* **2012**, 7, 12383.
- [22] J. Qiu, X. Liu, R. Chen, Q. Li, Y. Wang, P. Chen, L. Gan, S. J. Lee, D. Nordlund, Y. Liu, X. Yu, X. Bai, H. Li, L. Chen, *Adv. Funct. Mater.* **2020**, 30, 1909392.
- [23] D. T. Hallinan, A. Rausch, B. McGill, *Chem. Eng. Sci.* **2016**, 154, 34.
- [24] G. Homann, L. Stolz, J. Nair, I. C. Laskovic, M. Winter, J. Kasnatscheew, *Sci. Rep.* **2020**, 10, 4390.
- [25] J. Kasnatscheew, B. Streipert, S. Röser, R. Wagner, I. C. Laskovic, M. Winter, *Phys. Chem. Chem. Phys.* **2017**, 19, 16078.
- [26] J. R. Harding, C. V. Amanchukwu, P. T. Hammond, Y. Shao Horn, *J. Phys. Chem. C* **2015**, 119, 6947.
- [27] R. Nölle, K. Beltrop, F. Holtstiege, J. Kasnatscheew, T. Placke, M. Winter, *Mater. Today* **2020**, 32, 131.
- [28] A. J. Bard, L. R. Faulkner, *Electrochemical Methods Fundamentals and Applications*, Second Edition, John Wiley & Sons, Inc., New York, NY, USA **2001**.
- [29] T. Thompson, S. Yu, L. Williams, R. D. Schmidt, R. Garcia-Mendez, J. Wolfenstine, J. L. Allen, E. Kioupakis, D. J. Siegel, J. Sakamoto, *ACS Energy Lett.* **2017**, 2, 462.
- [30] J. T. S. Irvine, D. C. Sinclair, A. R. West, *Adv. Mater.* **1990**, 2, 132.
- [31] K. K. Kumar, M. Ravi, Y. Pavani, S. Bhavani, A. K. Sharma, V. V. R. N. Rao, *J. Non-Cryst. Solids* **2012**, 358, 3205.
- [32] L.-V. Daimay, N. B. Colthup, W. G. Fateley, J. G. Grasselli, *The Handbook of Infrared and Raman Characteristic Frequencies of Organic Molecules*, Academic Press, San Diego, New York, Boston, London, Sydney, Tokyo, Toronto **1991**.
- [33] I. Rey, P. Johansson, J. Lindgren, J. C. Lassègues, J. Grondin, L. Servant, *J. Phys. Chem. A* **1998**, 102, 3249.
- [34] K. Nie, X. Wang, J. Qiu, Y. Wang, Q. Yang, J. Xu, X. Yu, H. Li, X. Huang, L. Chen, *ACS Energy Lett.* **2020**, 5, 826.
- [35] Z. Li, Y. Zhao, W. E. Tenhaeff, *Chem. Mater.* **2021**, 33, 1927.
- [36] E. K. Plyler, *J. Res. Natl. Bur. Stand.* **1952**, 48, 281.
- [37] N. N. Sa'adun, R. Subramaniam, R. Kasi, *Sci. World J.* **2014**, 2014, 254215.
- [38] T. L. Barr, S. Seal, *J. Vac. Sci. Technol., A* **1995**, 13, 1239.
- [39] P. J. Linstrom, W. G. Mallard, *NIST Chemistry WebBook, NIST Standard Reference Database Number 69, International*, 69th ed., National Institute of Standards and Technology, Gaithersburg, MD, USA **2018**.
- [40] X. Yang, M. Jiang, X. Gao, D. Bao, Q. Sun, N. Holmes, H. Duan, S. Mukherjee, K. Adair, C. Zhao, J. Liang, W. Li, J. Li, Y. Liu, H. Huang, L. Zhang, S. Lu, Q. Lu, R. Li, C. V. Singh, X. Sun, *Energy Environ. Sci.* **2020**, 13, 1318.
- [41] F. Faglioni, B. V. Merinov, W. A. Goddard, B. Kozinsky, *Phys. Chem. Chem. Phys.* **2018**, 20, 26098.
- [42] S. P. Culver, R. Koerver, W. G. Zeier, J. Janek, *Adv. Energy Mater.* **2019**, 9, 1900626.
- [43] X. Dong, J. Yao, W. Zhu, X. Huang, X. Kuai, J. Tang, X. Li, S. Dai, L. Shen, R. Yang, L. Gao, J. Zhao, *J. Mater. Chem. A* **2019**, 7, 20262.
- [44] L. Stolz, G. Homann, M. Winter, J. Kasnatscheew, *Mater. Adv.* **2021**, 2, 3251.
- [45] E. J. Berg, P. Novák, *PSI Electrochemistry Laboratory - Annual Report* **2012**, 47.